Anomalous Floquet non-Hermitian skin effect in a ring resonator lattice

He Gao,[1] Haoran Xue,[2,*] Zhongming Gu,[3] Linhu Li,[4] Weiwei Zhu,[5] Zhongqing Su,[1] Jie Zhu,[3,†]
Baile Zhang,[2,6,‡] and Y. D. Chong[2,6,§]

[1]*Department of Mechanical Engineering, The Hong Kong Polytechnic University, Kowloon, Hong Kong SAR, China*
[2]*Division of Physics and Applied Physics, School of Physical and Mathematical Sciences, Nanyang Technological University, Singapore 637371, Singapore*
[3]*Institute of Acoustics, School of Physics Science and Engineering, Tongji University, Shanghai 200092, China*
[4]*Guangdong Provincial Key Laboratory of Quantum Metrology and Sensing & School of Physics and Astronomy, Sun Yat-Sen University (Zhuhai Campus), Zhuhai 519082, China*
[5]*Department of Physics, National University of Singapore, Singapore 117542, Singapore*
[6]*Centre for Disruptive Photonic Technologies, Nanyang Technological University, Singapore 637371, Singapore*

(Received 18 May 2022; revised 7 October 2022; accepted 12 October 2022; published 27 October 2022)

We present a one-dimensional coupled ring resonator lattice exhibiting a variant of the non-Hermitian skin effect (NHSE) that we call the anomalous Floquet NHSE. Unlike existing approaches to achieving the NHSE by engineering gain and loss on different ring segments, our design uses fixed on-site gain or loss in each ring. The anomalous Floquet NHSE is marked by the existence of skin modes at every value of the Floquet quasienergy, allowing for broadband asymmetric transmission. Varying the gain or loss induces a non-Hermitian topological phase transition, reversing the localization direction of the skin modes. An experimental implementation in an acoustic lattice yields good agreement with theoretical predictions, with a very broad relative bandwidth of around 40%.

DOI: 10.1103/PhysRevB.106.134112

I. INTRODUCTION

Non-Hermitian systems can exhibit a range of striking phenomena with no counterparts in the Hermitian regime [1–5]. The one that has perhaps attracted the most interest over the past two decades is parity-time ($\mathcal{PT}$) symmetry, which allows a non-Hermitian system to host real eigenvalues and non-Hermitian phase transitions [6]; this has been realized and extensively investigated in photonics, and other platforms such as acoustics, using classical gain and loss to implement non-Hermiticity [7–10]. Recently, much attention has been drawn to another non-Hermitian phenomenon called the non-Hermitian skin effect (NHSE) [11–15], whereby a non-Hermitian lattice hosts an extensive number of boundary-localized eigenmodes called skin modes. The NHSE is theoretically intriguing as it signifies a breakdown of Bloch's theorem for non-Hermitian systems [11–18] and is associated with exotic non-Hermitian bulk-boundary correspondences based on the windings of complex energy spectra [13,19–21]; moreover, it may have application possibilities in sensing [22,23] and lasing [24,25]. Over the past two years, experimental realizations of the NHSE have rapidly emerged in electric circuits [26–28], quantum walks [29,30], phononic metamaterials [31–35], optical-fiber-based synthetic lattices [36,37], and active particle systems [38]. A notable obstacle to such experimental studies is the fact that the simplest theories of the NHSE (though not all of them [39,40]) involve tight-binding models with nonreciprocal intersite couplings, which tend to be difficult to implement.

In this paper, we study an interesting form of the NHSE that arises in lattices of coupled ring resonators. We theoretically analyze and experimentally implement one-dimensional lattices of coupled ring resonators with on-site gain and loss, in a configuration that does not require placing gain or loss on different segments of some rings (which had been the approach adopted in earlier works to induce nonreciprocal intersite couplings [34,41–44]). Coupled-ring lattices have two key features relevant to the NHSE: (i) If waves experience negligible back reflection while propagating in the lattice (a standard assumption), certain lattice configurations allow the eigenmodes to split into two circulation sectors that are each effectively nonreciprocal [45–48]; (ii) in the strong-coupling regime, eigenmodes are solutions to a Floquet, rather than Hamiltonian, eigenproblem, and can deviate qualitatively from tight-binding models [49].

We show that our coupled-ring lattice exhibits an "anomalous Floquet NHSE" whereby the real part of the Floquet quasienergy winds through its entire 2π range—something that cannot occur in Hamiltonian models [11–18]. The skin modes manifest in the *entire* range of Floquet quasienergies, rather than a small interval corresponding to the bulk energy band. This behavior can potentially be used to achieve asymmetric transmission over a much larger bandwidth than in non-Floquet systems. As a proof of principle, we construct an acoustic lattice exhibiting the anomalous Floquet NHSE and demonstrate experimental results that are consistent with the theoretical model, and in quantitative agreement

---

[*] haoran001@e.ntu.edu.sg
[†] jiezhu@tongji.edu.cn
[‡] blzhang@ntu.edu.sg
[§] yidong@ntu.edu.sg

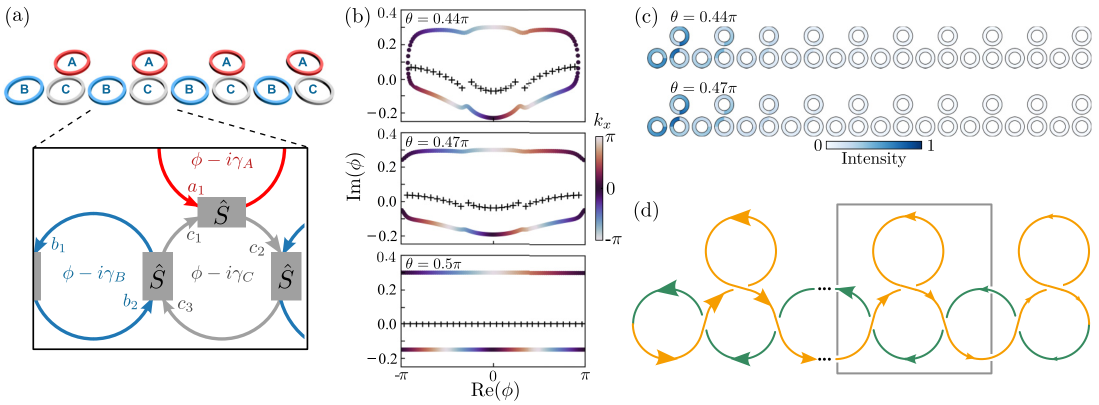

FIG. 1. (a) Schematic of a finite lattice of coupled ring resonators (top) and a close-up view (bottom). One round trip in each ring multiplies the wave amplitude by $\exp[i(\phi - i\gamma_{A,B,C})]$. The phase shift ϕ is interpreted as a Floquet quasienergy. The wave coefficients at six points in the unit cell are denoted by $(a_1, b_1, b_2, c_1, c_2, c_3)$. (b) Complex quasienergy spectrum under PBCs (colored dots) and OBCs with a lattice of ten unit cells (black pluses) for $\theta \in \{0.44\pi, 0.47\pi, 0.5\pi\}$. (c) Intensity profiles, summed over all eigenmodes, for the lattices with OBCs and $\theta \in \{0.44\pi, 0.47\pi\}$. Both of these cases host skin modes, despite the qualitative differences in the PBC spectra. (d) Wave propagation patterns under perfect coupling, $\theta = 0.5\pi$. The gray rectangle marks one unit cell. If an OBC mode's right-moving path (orange) is damped, then its left-moving path (green) is amplified and the mode profile is exponentially localized to the left, as indicated by the sizes of the arrows. In (b) and (c), the gain or loss parameters are $\gamma_A = -0.6$ and $\gamma_B = \gamma_C = 0.3$.

with full-wave simulations, over a ~40% relative frequency bandwidth. This design may also be useful for achieving broadband NHSE, and related phenomena, in platforms such as microwave photonics [50,51] and nanophotonics [45,52–54].

II. THEORY

Consider the one-dimensional lattice shown in Fig. 1(a), with each unit cell consisting of three distinct coupled ring resonators. Waves propagating in each ring acquire phase shifts as well as experiencing amplitude growth (decay) due to gain (loss). For the rings drawn in red, blue, and gray in Fig. 1(a), and labeled $\{A, B, C\}$, one round trip multiplies the complex wave amplitude by $\exp[i(\phi - i\gamma_{A,B,C})]$. If ϕ is real, it corresponds to the round-trip phase shift in each ring, while positive (negative) values of $\gamma_{A,B,C}$ correspond to gain (loss) in the respective rings. We consider only one of the two choices of circulation directions in the lattice—say, counterclockwise in the A and B rings and clockwise in the C rings—with no "spin flipping" [45]. This restriction to one circulation sector effectively breaks reciprocity [45–48]. For simplicity, we let all rings share the same ϕ parameter, which is interpreted as a Floquet quasienergy [46,47]. However, the behaviors discussed below generalize to rings of different ϕ; as an example, in the Supplemental Material we describe the case where the A and B rings are antiresonant with the C rings [55]. Note also that each ring is assumed to have uniform gain or loss (or neither), unlike previously studied non-Hermitian coupled-ring models that have gain or loss on different parts of each ring [34,41–43].

Wave propagation within the lattice can be modeled with the transfer matrix method [45–48]. As shown in Fig. 1(a), we let $\{a_1, b_1, b_2, c_1, c_2, c_3\}$ denote the complex wave amplitudes at six points in the unit cell, just before the coupling regions between adjacent rings. The coupling is described by a scattering matrix $\hat{S} = \cos(\theta) - i\hat{\sigma}_1 \sin\theta$, where $\hat{\sigma}_1$ is a Pauli matrix and the angle θ describes the coupling strength, with $\theta = \pi/2$ corresponding to perfect coupling.

For a given set of source-free boundary conditions, such as periodic boundary conditions (PBCs) or open boundary conditions (OBCs), the scattering and coupling equations can be cast as a Floquet eigenproblem of the form $\hat{U}|\Psi\rangle = e^{-i\phi}|\Psi\rangle$, where $\hat{U}$ is an evolution operator and $|\Psi\rangle$ is a vector of complex wave amplitudes [45–47,55]. Physically, Re[ϕ] describes the round-trip phase shifts in each ring, and Im[ϕ] is an additional gain or loss applied to each ring (on top of $\gamma_{A,B,C}$) to produce a self-consistent wave pattern in the lattice. In a real system, ϕ is typically proportional to the operating frequency, though the other parameters $\gamma_{A,B,C}$ and θ may also vary with frequency.

Figure 1(b) shows the complex quasienergy spectra for $\gamma_A = -0.6$, $\gamma_B = \gamma_C = 0.3$, and different values of θ. In each plot, the colored markers correspond to PBCs, and the black crosses correspond to OBCs for a lattice of ten unit cells with the same termination conditions as in Fig. 1(a). For $\theta = 0.44\pi$ [upper panel of Fig. 1(b)], the behavior is similar to previous non-Hermitian Hamiltonian models exhibiting the NHSE [11–18]: The quasienergies for PBCs form a loop with nonzero point gap winding, while the quasienergies for OBCs form an arc enclosed by and connecting to the loop. The OBC eigenmodes exhibit the NHSE, as shown in the upper panel of Fig. 1(c).

With a larger coupling angle, $\theta = 0.47\pi$, the complex quasienergy spectrum is qualitatively different. As shown in the middle panel of Fig. 1(b), under both PBCs and OBCs, the quasienergies wrap across the entire range of Re[ϕ] $\in [-\pi, \pi]$, and the arc of OBC quasienergies never meets the PBC quasienergies. Nonetheless, in this regime there exists a macroscopic number of skin modes, as shown in the lower panel of Fig. 1(c).

This type of complex spectrum is made possible by the fact that the present model is a Floquet system—i.e., it is governed by a (nonunitary) evolution operator $\hat{U}$ rather than a (non-Hermitian) Hamiltonian, so that Re[ϕ] is an angle variable [47,49]. In other Floquet models, similar quasienergy wrappings have been shown to give rise to so-called anomalous Floquet insulators [49–51,56] and other anomalous Floquet phases [57,58]. Similarly, we call the present behavior the "anomalous Floquet NHSE."

Because the skin modes have quasienergies spanning the entire range of Re[ϕ] $\in [-\pi, \pi]$, the anomalous Floquet NHSE is a broadband phenomenon. Instead of using the standard definition of point gap winding [13,19–21], it can be characterized by [55]

$$\nu(\phi_r) = \int_{\mathrm{BZ}} \frac{dk_x}{2\pi} \frac{d}{dk_x} \arg\det[\hat{U} - e^{-i\phi_r}], \tag{1}$$

which describes the winding of $e^{-i\phi}$ (not ϕ) around a reference point $e^{-i\phi_r}$ (BZ refers to the Brillouin zone). All three cases in Fig. 1(b) have $\nu(0) = 1$, consistent with the occurrence of skin modes.

The physical origin of the anomalous Floquet NHSE can be understood using the extremal case of $\theta = 0.5\pi$, or perfect inter-ring coupling. As shown in the bottom plot of Fig. 1(b), under PBCs there are two quasienergy bands with constant Im[ϕ], whereas all the OBC modes have the same Im[ϕ]. Perfect inter-ring coupling causes wave trajectories to form two distinct paths in the bulk, as shown in Fig. 1(d). Under PBCs, the paths are completely decoupled; for the right-moving path, the wave amplitudes are multiplied by $\exp[i(2\phi - i\Gamma_R)]$ per unit cell, where $\Gamma_R = \gamma_A + (\gamma_B + \gamma_C)/2$, and applying the Bloch condition yields the dispersion relation $\phi = k/2 + i\Gamma_R/2$, where k is the Bloch wave number with the lattice period normalized to unity. The left-moving wave amplitudes are multiplied by $\exp[i(\phi - i\Gamma_L)]$ per unit cell, where $\Gamma_L = (\gamma_B + \gamma_C)/2$, so their dispersion relation is $\phi = -k + i\Gamma_L$. Under OBCs, the two paths meet at the ends of the lattice, as seen in Fig. 1(d). A self-consistent wave pattern must have no net gain or loss after each round trip, so Im[ϕ] $= (\Gamma_L + \Gamma_R)/3 = (\gamma_A + \gamma_B + \gamma_C)/3$, consistent with the complex quasienergy spectrum shown in Fig. 1(b). If the left-moving (right-moving path) in an OBC mode is amplified (damped), the mode profile grows exponentially to the left, as indicated by the arrow sizes in Fig. 1(d). Such a formation picture of the skin modes under OBCs applies to all ϕ in the perfect coupling case, thus leading to the anomalous Floquet NHSE.

We have chosen a coupling strength and gain or loss configuration that is feasible for experiments (e.g., rings in the same row have the same gain or loss). For other parameter choices, we observe similar behaviors, including other instances of the anomalous Floquet NHSE. The PBC spectrum can even exhibit multiple loops with different winding directions, resulting in skin modes localized at different boundaries, consistent with the above bulk-boundary correspondence principle [55].

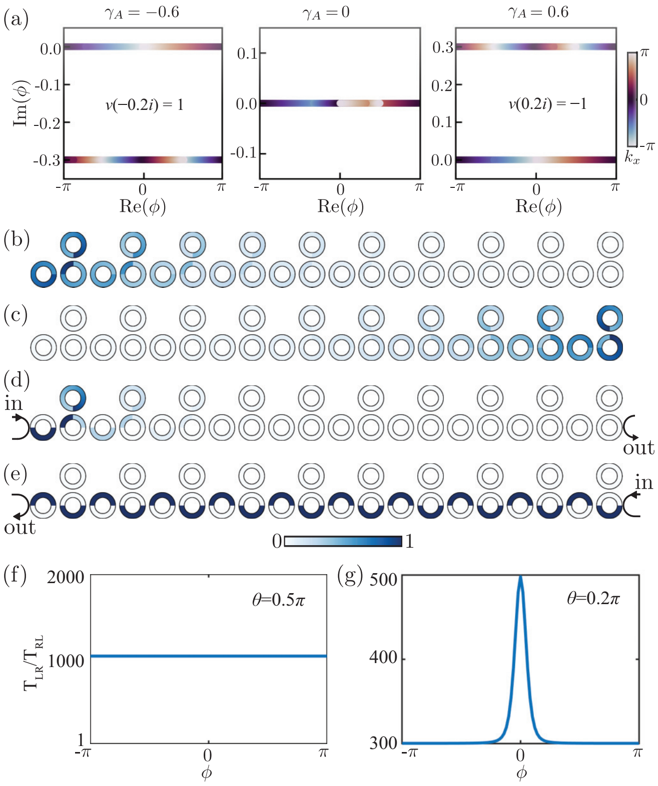

FIG. 2. (a) Spectra for a lattice under PBCs with gain and loss parameters: $\gamma_B = \gamma_C = 0$, $\gamma_A = -0.6, 0, 0.6$ (left to right). (b) and (c) Profile of a typical skin mode in a lattice under OBCs, with $\gamma_B = \gamma_C = 0$, and (b) $\gamma_A = -0.6$, (c) $\gamma_A = 0.6$. (d) and (e) Field distributions when exciting the lattice from the left and the right, respectively. (f) and (g) Plots of transmission ratio $\mathrm{T_{LR}/T_{RL}}$ against ϕ for $\theta = 0.5\pi$ and $\theta = 0.2\pi$, respectively. Here, $\mathrm{T_{LR}}$ ($\mathrm{T_{RL}}$) denotes transmission from right to left (left to right). In (d) and (e), the gain or loss parameters are the same as in (a), and the input and output couplings are $\theta_{\mathrm{in}} = \theta_{\mathrm{out}} = 0.5\pi$.

Moreover, gain and loss can induce a topological transition whereby the Floquet point gap windings reverse direction, and the skin modes correspondingly switch boundaries. To demonstrate this, consider a lattice with the following parameters: $\gamma_B = \gamma_C = 0$ and $\theta = 0.5\pi$. In addition, we introduce a variable γ_A that can be tuned to achieve the topological transition. Figure 2(a) shows the spectra under PBCs as γ_A is increased from -0.6 to 0.6. For $\gamma_A = -0.6$, the PBC spectrum consists of two branches, as shown in the left panel of Fig. 2(a). We find $\nu = 1$ (for $\phi_r = -0.2i$), and the skin modes are localized to the left boundary as shown in Fig. 2(b). Upon increasing γ_A, the two branches of PBC quasienergies approach each other, meeting at $\gamma_A = 0$ as shown in the middle panel of Fig. 2(a). This is the phase transition point. As γ_A is further increased, the PBC spectrum again splits into two branches with $\nu = -1$ (for $\phi_r = 0.2i$), as shown in the right panel of Fig. 2(a). The OBC modes are now skin modes localized on the right boundary, as shown in Fig. 2(c). Thus our Floquet model enables the active control of the NHSE, which may be useful for reconfigurable devices based on optical platforms where gain and loss can be tuned by external pumping [52].

Thus far, we have investigated how the model behaves under source-free conditions. In Figs. 2(d) and 2(e), we study the transmission properties when inputs and outputs are attached to the ends of the lattice. The lattice parameters are the same as in the left panel of Fig. 2(a); the couplings between the couplers and the lattice are set to 0.5π (i.e., perfect coupling). As shown in Figs. 2(d) and 2(e), the wave is continuously

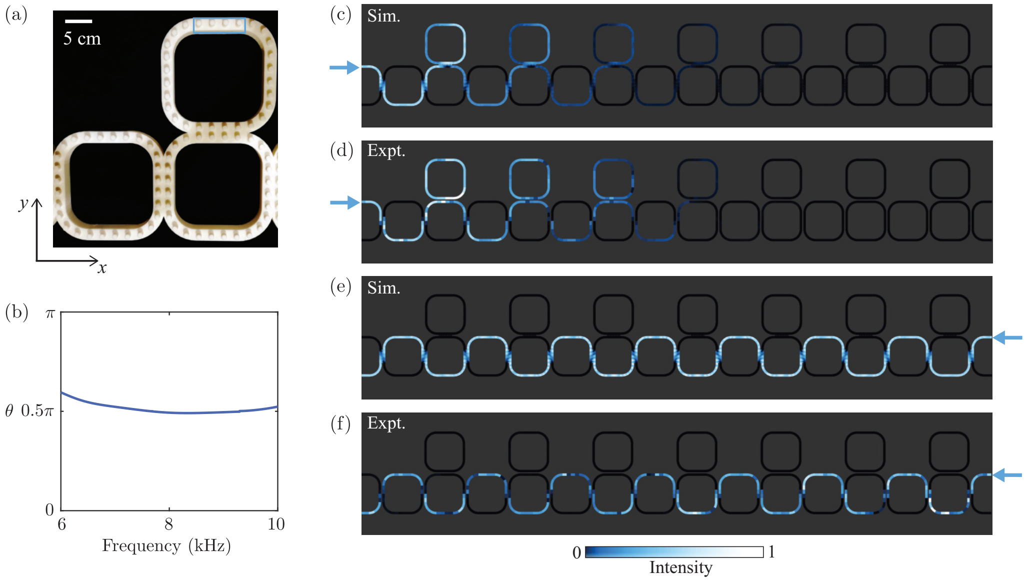

FIG. 3. (a) Photograph of one unit cell in the experimental sample. (b) Plot of effective coupling angle θ against frequency, extracted from full-wave numerical simulations as described in the Supplemental Material [55]. (c)–(f) Full-wave acoustic simulations and experimental measurements of the acoustic intensity under (c) and (d) left incidence and (e) and (f) right incidence. The excitation frequency is 8000 Hz. In (d) and (f), we multiply the measurement results by a factor of $\exp(\alpha l)$, where α is a decay factor and l is the path length, to compensate for background losses [55]. In the full-wave simulations, intrinsic losses are absent, and the additional loss in the A ring is implemented as a nonzero imaginary part in the sound speed. The experiment and simulations can be described by the Floquet model with $\gamma_A = -0.35$, $\gamma_B = 0$, and $\gamma_C = 0$.

attenuated (unattenuated) when transmitted left to right (right to left). This is consistent with the localization of the skin modes and with the previously discussed differences in relative gain between left- and right-moving paths. Furthermore, such an asymmetric transmission behavior is broadband in the anomalous Floquet NHSE case [Fig. 2(f)]. When the coupling is decreased and the skin modes only exist for a small range of ϕ, the broadband property no longer holds [Fig. 2(g)].

III. EXPERIMENT

We performed a proof-of-principle experimental demonstration using an acoustic lattice. As shown in Fig. 3(a), the lattice unit cell consists of three coupled rings with the same dimensions. Each ring is filled with air and surrounded by rigid walls, with adjacent rings connected by small channels (see Supplemental Material for detailed structural parameters [55]). The couplings are optimized so that the effective θ, derived from full-wave simulations [55], is approximately 0.5π over a wide range of frequencies, as shown in Fig. 3(b).

Unlike the previously discussed theoretical models, the experimental sample is purely lossy. There are two sources of loss: The first is intrinsic loss due to material absorption, which is the same for all rings. The second type of loss comes from the intentional introduction of absorbing materials to a segment of each A ring, indicated by the blue box in Fig. 3(a).

The lattice is excited by a monochromatic signal with a frequency of 8000 Hz incident from the left or right end, as indicated by the blue arrows in Figs. 3(c)–3(f). We probe the acoustic intensities at various positions by inserting microphones into the rings, with a step of 28 mm (see Supplemental Material for more details on the measurement [55]). For ease of visualization, the measured intensities in Figs. 3(d) and 3(f) are compensated by multiplying the measured intensity by a factor $e^{\alpha l}$, where α is a decay factor induced by the background loss and l is the propagation length [55]. The uncompensated intensity fields are shown in the Supplemental Material [55].

When the signal is injected from the left, the acoustic intensity attenuates rapidly, as demonstrated in Figs. 3(c) and 3(d). By contrast, if the signal is injected from the right, the attenuation is negligible, as seen in Figs. 3(e) and 3(f). This is consistent with the behavior discussed in Figs. 2(d) and 2(e). The asymmetric transmission is experimentally observed in a frequency window ranging from 6500 to 10 000 Hz (i.e., a relative bandwidth of $\sim$40%), consistent with the theoretical expectations that the anomalous Floquet NHSE should be broadband (experimental results at other frequencies are given in the Supplemental Material [55]).

IV. DISCUSSION

We have shown theoretically and experimentally that the NHSE can occur in a lattice of coupled ring resonators. By analyzing lattice modes as Floquet eigenstates [45–47], we found a variant of the NHSE, the anomalous Floquet NHSE, in which skin modes exist at every quasienergy. This phenomenon arises from the special features of Floquet band structures, which had previously been exploited in anomalous Floquet insulators to produce broadband and extraordinarily robust topological states [56]. Similarly, the anomalous Floquet NHSE allows for broadband asymmetric transmission enabled by skin modes.

We note that there have been previous proposals to realize the nonanomalous NHSE in coupled-ring lattices, by

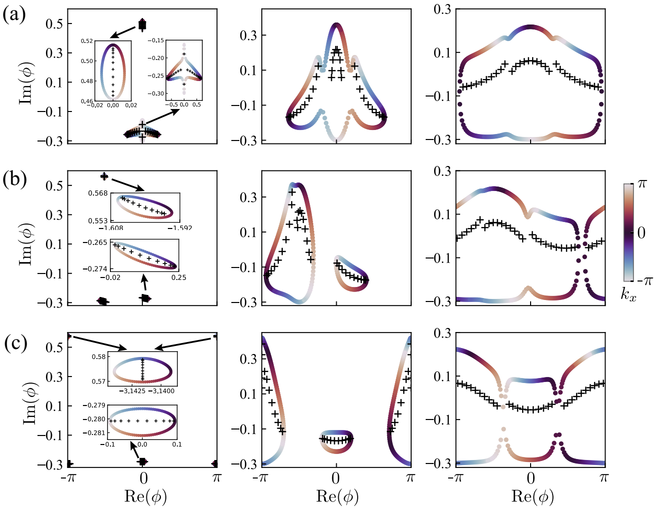

FIG. 4. PBC and OBC spectra for the lattice with the round trip phases being (a) $\epsilon_A = \epsilon_B = \phi$, (b) $\epsilon_A = \epsilon_B = \phi + \pi/2$ and $\epsilon_A = \epsilon_B = \phi + \pi$, respectively. The coupling strengths are $\theta = 0.1\pi, 0.3\pi, 0.45\pi$ from the left column to the right column. The gain and loss parameters are $\gamma_A = 0.6$, $\gamma_B = \gamma_C = -0.3$.

designating certain rings as "coupling rings" with varying gain or loss on different arms [34,41–43]. By comparison, our design assigns to each ring a certain level of gain or loss, and does not require gain or loss engineering on ring segments. It may thus be easier to implement, especially on other platforms such as photonics. There, our model may be helpful for realizing NHSE-aided lasing [24,25] and for studying the interplay of the NHSE with other non-Hermitian effects [4] or nonlinearities [59–61]. The coupled-ring model can also be mapped to helical waveguide arrays [62] or temporally modulated Floquet systems [49]. Finally, it would be interesting to generalize the lattice to two or higher dimensions [55], in order to investigate higher-dimensional versions of the anomalous Floquet NHSE.

ACKNOWLEDGMENTS

H.G., Z.G., Z.S., and J.Z. acknowledge support from the Research Grants Council of Hong Kong SAR (Grants No. 15205219, No. C6013-18G, and No. AoE/P-502/20) and the National Natural Science Foundation of China (Grant No. 11774297). H.X., B.Z., and Y.D.C. acknowledge support from Singapore MOE Academic Research Fund Tier 3 Grant No. MOE2016-T3-1-006, Tier 2 Grant No. MOE2019-T2-2-085, and Tier 1 Grant No. RG148/20 and the Singapore National Research Foundation (NRF) Competitive Research Program (CRP) (Grant No. NRF-CRP23-2019-0007). H.G. and H.X. contributed equally to this work.

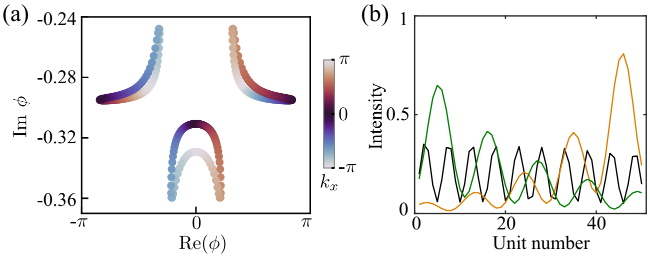

FIG. 5. (a) Spectrum for the lattice under PBCs with system parameters $\gamma_A = -0.3$, $\gamma_B = -0.6$, $\gamma_C = 0$, $\theta = 0.4\pi$, $\epsilon_A = \epsilon_B = \phi$. (b) Intensity profiles for the selected three modes for a lattice with 50 unit cells under OBCs.

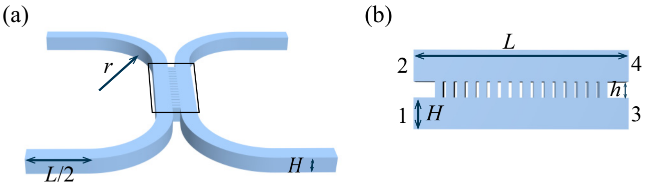

FIG. 6. (a) Two coupled U-shaped waveguides. (b) Top view of the structure indicated by the black box in (a).

APPENDIX A: MORE NUMERICAL RESULTS

As shown in Fig. 4, the PBC and OBC spectra always differ significantly from each other, indicating the existence of the NHSE. In Fig. 4, the round-trip phases are set to be $\epsilon_A = \epsilon_B = \phi$, $\epsilon_A = \epsilon_B = \phi + \pi/2$, and $\epsilon_A = \epsilon_B = \phi + \pi$ for Figs. 4(a), 4(b), and 4(c), respectively. The coupling strengths are $\theta = 0.1\pi, 0.3\pi, 0.45\pi$ from the left column to the right column. The gain or loss parameters are $\gamma_A = 0.6$, $\gamma_B = \gamma_C = -0.3$. Moreover, under certain parameters, the PBC spectrum can form loops associated with opposite windings, thus giving rising to skin modes localized at opposite boundaries. An example of this is given in Fig. 5.

APPENDIX B: DETAILS OF FULL-WAVE SIMULATIONS

Figure 6(a) illustrates two coupled U-shaped waveguides, which act as the basic element of the coupled-ring lattice in the simulations. Their structural parameters are $L = 96$ mm, $r = 56$ mm, and $H = 14$ mm. Each ring consists of two symmetrical U-shaped waveguides. The rings are coupled with a grating [Fig. 6(b)], which is composed of 16 thin channels with the height h, width, and period being 7, 3.5, and 4.9 mm, respectively. The coupling strength profile and simulated field

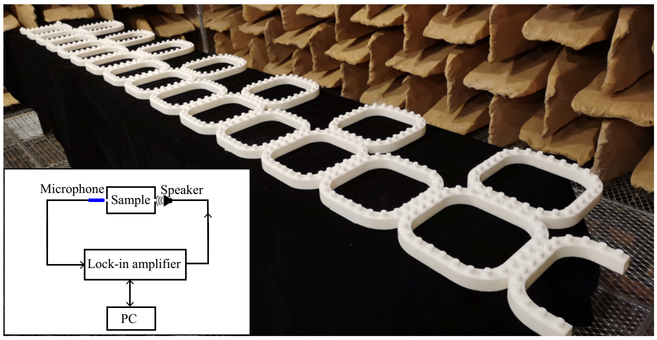

FIG. 7. Photo of the printed sample. It is composed of seven unit cells. The left and right sides of the sample are coupled with a U-shaped waveguide for external excitation. The inset is an illustration of the experimental setup.

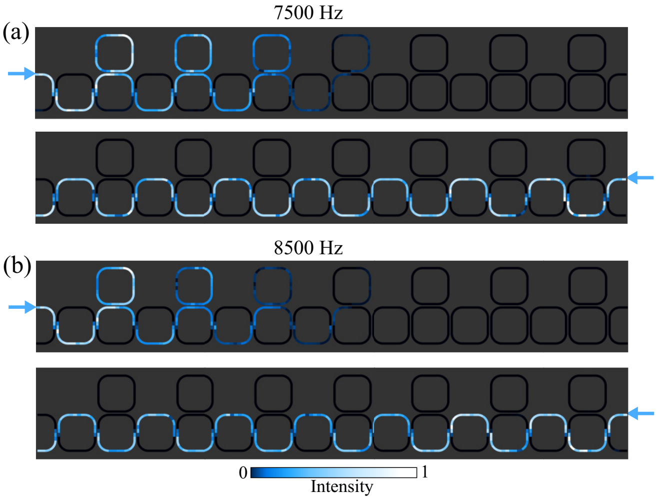

FIG. 8. Experimental measurements of the acoustic intensity under left and right incidence at (a) 7500 Hz and (b) 8500 Hz, respectively. We multiply the measurement results by a factor of $\exp(\alpha l)$, where α is a decay factor and l is the path length, to compensate for background losses.

distributions in Fig. 3 are numerically calculated with the pressure-acoustics module of COMSOL MULTIPHYSICS. The density and real part of the sound speed of the background medium are set to be 1.21 $\mathrm{kg/m^3}$ and 343 m/s, respectively. In the simulation of Fig. 3(c), we also add a nonzero number to the imaginary part of the sound speed in the A ring to account for the additional loss.

The numerical procedures to extract the coupling angle θ are as follows. Consider the structure shown in Fig. 6(b), where the acoustic pressure at the four ports is denoted by (p_1, p_2, p_3, p_4). Supposing the sound wave to be incident on this structure from port 1 with pressure p_i, we have $|\theta| = \mathrm{atan}(p_4/p_3)$. When $p_3/p_i > 0$ $(p_3/p_i < 0)$, the coupling strength $\theta = |\theta|$ $(\theta = \pi - |\theta|)$ [58]. Based on this, the evolution of coupling strength versus frequency is numerically obtained, as presented in Fig. 3(b).

APPENDIX C: DETAILS OF THE EXPERIMENTS AND DATA PROCESSING

The experimental sample is fabricated via three-dimensional (3D) printing, as shown in Fig. 7. It is composed of seven unit cells, each of which has two site rings and one linking ring. A U-shaped waveguide is respectively coupled to the two ends of the structure for inputting the sound signal. An array of small holes are drilled on one side of the sample for detecting the sound signal inside the sample. During the measurements, only one hole is left open for placing the microphone, and plugs are inserted in the rest of the holes.

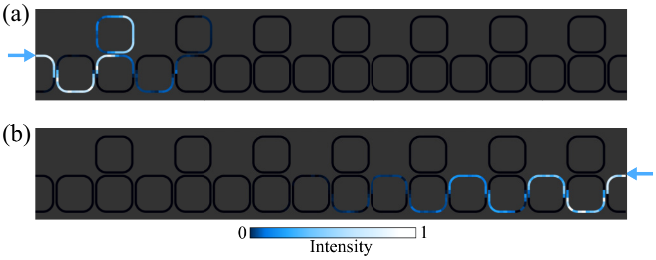

FIG. 9. Measured acoustic intensity fields without the compensation under (a) left incidence and (b) right incidence.

The excitation signal is generated by a loudspeaker controlled by the lock-in amplifier. For different excitation directions, the speaker is accordingly placed on one of the four ports on the two ends. The acoustic signal within the sample is measured by a 1/4-in. microphone (Brüel & Kjær, type 4935) that was placed in the small holes and then was transferred to the lock-in amplifier connected to a computer through a conditioning amplifier (Brüel & Kjær, 64 NEXUS type 2693A). This experimental setup is illustrated in the inset of Fig. 7.

We first measured the acoustic intensity profile for the ring lattice without any additional loss. The effective loss factor of the intrinsic background dissipation can be extracted by fitting the measured intensity to the curve $I_0 e^{-\alpha l}$, where I_0 is the input intensity, l is the propagation length, and α is the decay factor. α is estimated to be 0.0081 $\mathrm{cm^{-1}}$. To compensate the background loss, we multiply the experimental data by $e^{\alpha l}$, which yields the results shown in Figs. 3(d) and 3(f).

APPENDIX D: MORE EXPERIMENTAL RESULTS

Here we display more experimental results at different frequencies to demonstrate the broadband nature of the anomalous Floquet NHSE. Figures 8(a) and 8(b) show the measured acoustic intensity fields with the excitation frequency at 7500 and 8500 Hz, respectively. As can be seen, the propagation distance for the wave incident from the left side is much shorter (counting the number of units) than that for the wave incident from the right side, which is similar to what is observed at 8000 Hz [see Figs. 3(c)–3(f)]. In fact, the asymmetric transmission feature can be observed in the entire frequency window from 6800 to 10 000 Hz, in which the coupling strength θ is around 0.5π.

The measured acoustic intensity fields without the compensation are plotted in Fig. 9. We can still see that the propagation distance for the wave incident from the left side is much shorter (counting the number of units) than that for the wave incident from the right side, which demonstrates the asymmetric transmission of our design, consistent with the results in Fig. 3 (though less clear).

---

[1] L. Feng, R. El-Ganainy, and L. Ge, Non-Hermitian photonics based on parity–time symmetry, Nat. Photonics **11**, 752 (2017).
[2] R. El-Ganainy, K. G. Makris, M. Khajavikhan, Z. H. Musslimani, S. Rotter, and D. N. Christodoulides, Non-Hermitian physics and PT symmetry, Nat. Phys. **14**, 11 (2018).
[3] M.-A. Miri and A. Alù, Exceptional points in optics and photonics, Science **363**, eaar7709 (2019).

[4] V. V. Konotop, J. Yang, and D. A. Zezyulin, Nonlinear waves in PT-symmetric systems, Rev. Mod. Phys. **88**, 035002 (2016).

[5] E. J. Bergholtz, J. C. Budich, and F. K. Kunst, Exceptional topology of non-Hermitian systems, Rev. Mod. Phys. **93**, 015005 (2021).

[6] C. M. Bender and S. Boettcher, Real Spectra in Non-Hermitian Hamiltonians Having $\mathcal{PT}$ Symmetry, Phys. Rev. Lett. **80**, 5243 (1998).

[7] A. Guo, G. J. Salamo, D. Duchesne, R. Morandotti, M. Volatier-Ravat, V. Aimez, G. A. Siviloglou, and D. N. Christodoulides, Observation of $\mathcal{PT}$-Symmetry Breaking in Complex Optical Potentials, Phys. Rev. Lett. **103**, 093902 (2009).

[8] C. E. Rüter, K. G. Makris, R. El-Ganainy, D. N. Christodoulides, M. Segev, and D. Kip, Observation of parity–time symmetry in optics, Nat. Phys. **6**, 192 (2010).

[9] H. Hodaei, M.-A. Miri, M. Heinrich, D. N. Christodoulides, and M. Khajavikhan, Parity-time–symmetric microring lasers, Science **346**, 975 (2014).

[10] L. Feng, Z. J. Wong, R.-M. Ma, Y. Wang, and X. Zhang, Single-mode laser by parity-time symmetry breaking, Science **346**, 972 (2014).

[11] V. M. Alvarez, J. B. Vargas, and L. F. Torres, Non-Hermitian robust edge states in one dimension: Anomalous localization and eigenspace condensation at exceptional points, Phys. Rev. B **97**, 121401(R) (2018).

[12] Y. Xiong, Why does bulk boundary correspondence fail in some non-Hermitian topological models, J. Phys. Commun. **2**, 035043 (2018).

[13] Z. Gong, Y. Ashida, K. Kawabata, K. Takasan, S. Higashikawa, and M. Ueda, Topological Phases of Non-Hermitian Systems, Phys. Rev. X **8**, 031079 (2018).

[14] S. Yao and Z. Wang, Edge States and Topological Invariants of Non-Hermitian Systems, Phys. Rev. Lett. **121**, 086803 (2018).

[15] F. K. Kunst, E. Edvardsson, J. C. Budich, and E. J. Bergholtz, Biorthogonal Bulk-Boundary Correspondence in Non-Hermitian Systems, Phys. Rev. Lett. **121**, 026808 (2018).

[16] T. E. Lee, Anomalous Edge State in a Non-Hermitian Lattice, Phys. Rev. Lett. **116**, 133903 (2016).

[17] S. Yao, F. Song, and Z. Wang, Non-Hermitian Chern Bands, Phys. Rev. Lett. **121**, 136802 (2018).

[18] C. H. Lee and R. Thomale, Anatomy of skin modes and topology in non-Hermitian systems, Phys. Rev. B **99**, 201103(R) (2019).

[19] N. Okuma, K. Kawabata, K. Shiozaki, and M. Sato, Topological Origin of Non-Hermitian Skin Effects, Phys. Rev. Lett. **124**, 086801 (2020).

[20] K. Zhang, Z. Yang, and C. Fang, Correspondence between Winding Numbers and Skin Modes in Non-Hermitian Systems, Phys. Rev. Lett. **125**, 126402 (2020).

[21] D. S. Borgnia, A. J. Kruchkov, and R.-J. Slager, Non-Hermitian Boundary Modes and Topology, Phys. Rev. Lett. **124**, 056802 (2020).

[22] J. C. Budich and E. J. Bergholtz, Non-Hermitian Topological Sensors, Phys. Rev. Lett. **125**, 180403 (2020).

[23] A. McDonald and A. A. Clerk, Exponentially-enhanced quantum sensing with non-Hermitian lattice dynamics, Nat. Commun. **11**, 5382 (2020).

[24] S. Longhi, Non-Hermitian gauged topological laser arrays, Ann. Phys. (Berlin) **530**, 1800023 (2018).

[25] B. F. Zhu, Q. Wang, D. Leykam, H. R. Xue, Q. J. Wang, and Y. D. Chong, Anomalous Single-Mode Lasing Induced by Nonlinearity and the Non-Hermitian Skin Effect, Phys. Rev. Lett. **129**, 013903 (2022).

[26] T. Helbig, T. Hofmann, S. Imhof, M. Abdelghany, T. Kiessling, L. Molenkamp, C. Lee, A. Szameit, M. Greiter, and R. Thomale, Generalized bulk–boundary correspondence in non-Hermitian topolectrical circuits, Nat. Phys. **16**, 747 (2020).

[27] S. Liu, R. Shao, S. Ma, L. Zhang, O. You, H. Wu, Y. J. Xiang, T. J. Cui, and S. Zhang, Non-Hermitian skin effect in a non-Hermitian electrical circuit, Research **2021**, 5608038 (2021).

[28] D. Zou, T. Chen, W. He, J. Bao, C. H. Lee, H. Sun, and X. Zhang, Observation of hybrid higher-order skin-topological effect in non-Hermitian topolectrical circuits, Nat. Commun. **12**, 7201 (2021).

[29] L. Xiao, T. Deng, K. Wang, G. Zhu, Z. Wang, W. Yi, and P. Xue, Non-Hermitian bulk–boundary correspondence in quantum dynamics, Nat. Phys. **16**, 761 (2020).

[30] L. Xiao, T. Deng, K. Wang, Z. Wang, W. Yi, and P. Xue, Observation of Non-Bloch Parity-Time Symmetry and Exceptional Points, Phys. Rev. Lett. **126**, 230402 (2021).

[31] M. Brandenbourger, X. Locsin, E. Lerner, and C. Coulais, Non-reciprocal robotic metamaterials, Nat. Commun. **10**, 4608 (2019).

[32] A. Ghatak, M. Brandenbourger, J. van Wezel, and C. Coulais, Observation of non-Hermitian topology and its bulk–edge correspondence in an active mechanical metamaterial, Proc. Natl. Acad. Sci. USA **117**, 29561 (2020).

[33] Y. Chen, X. Li, C. Scheibner, V. Vitelli, and G. Huang, Realization of active metamaterials with odd micropolar elasticity, Nat. Commun. **12**, 5935 (2021).

[34] X. Zhang, Y. Tian, J.-H. Jiang, M.-H. Lu, and Y.-F. Chen, Observation of higher-order non-Hermitian skin effect, Nat. Commun. **12**, 5377 (2021).

[35] L. Zhang, Y. Yang, Y. Ge, Y.-J. Guan, Q. Chen, Q. Yan, F. Chen, R. Xi, Y. Li, D. Jia, S.-Q. Yuan, H.-X. Sun, H. Chen, and B. Zhang, Acoustic non-Hermitian skin effect from twisted winding topology, Nat. Commun. **12**, 6297 (2021).

[36] S. Weidemann, M. Kremer, T. Helbig, T. Hofmann, A. Stegmaier, M. Greiter, R. Thomale, and A. Szameit, Topological funneling of light, Science **368**, 311 (2020).

[37] K. Wang, A. Dutt, K. Y. Yang, C. C. Wojcik, J. Vučković, and S. Fan, Generating arbitrary topological windings of a non-Hermitian band, Science **371**, 1240 (2021).

[38] L. S. Palacios, S. Tchoumakov, M. Guix, I. Pagonabarraga, S. Sánchez, and A. G Grushin, Guided accumulation of active particles by topological design of a second-order skin effect, Nat. Commun. **12**, 4691 (2021).

[39] Y. Yi and Z. Yang, Non-Hermitian Skin Modes Induced by On-Site Dissipations and Chiral Tunneling Effect, Phys. Rev. Lett. **125**, 186802 (2020).

[40] K. Zhang, Z. Yang, and C. Fang, Universal non-Hermitian skin effect in two and higher dimensions, Nat. Commun. **13**, 2496 (2022).

[41] S. Longhi, D. Gatti, and G. Della Valle, Robust light transport in non-Hermitian photonic lattices, Sci. Rep. **5**, 13376 (2015).

[42] X. Zhu, H. Wang, S. K. Gupta, H. Zhang, B. Xie, M. Lu, and Y. Chen, Photonic non-Hermitian skin effect and non-Bloch bulk-boundary correspondence, Phys. Rev. Res. **2**, 013280 (2020).

[43] Z. Lin, S. Ke, X. Zhu, and X. Li, Square-root non-Bloch topological insulators in non-Hermitian ring resonators, Opt. Express **29**, 8462 (2021).

[44] H. Liu, J.-S. You, S. Ryu, and I. C. Fulga, Supermetal-insulator transition in a non-Hermitian network model, Phys. Rev. B **104**, 155412 (2021).

[45] M. Hafezi, S. Mittal, J. Fan, A. Migdall, and J. Taylor, Imaging topological edge states in silicon photonics, Nat. Photonics **7**, 1001 (2013).

[46] G. Q. Liang and Y. D. Chong, Optical Resonator Analog of a Two-Dimensional Topological Insulator, Phys. Rev. Lett. **110**, 203904 (2013).

[47] M. Pasek and Y. D. Chong, Network models of photonic Floquet topological insulators, Phys. Rev. B **89**, 075113 (2014).

[48] D. Leykam, S. Mittal, M. Hafezi, and Y. D. Chong, Reconfigurable Topological Phases in Next-Nearest-Neighbor Coupled Resonator Lattices, Phys. Rev. Lett. **121**, 023901 (2018).

[49] M. S. Rudner, N. H. Lindner, E. Berg, and M. Levin, Anomalous Edge States and the Bulk-Edge Correspondence for Periodically Driven Two-Dimensional Systems, Phys. Rev. X **3**, 031005 (2013).

[50] W. Hu, J. C. Pillay, K. Wu, M. Pasek, P. P. Shum, and Y. D. Chong, Measurement of a Topological Edge Invariant in a Microwave Network, Phys. Rev. X **5**, 011012 (2015).

[51] F. Gao, Z. Gao, X. Shi, Z. Yang, X. Lin, H. Xu, J. D. Joannopoulos, M. Soljačić, H. Chen, L. Lu, Y. Chong, and B. Zhang, Probing topological protection using a designer surface plasmon structure, Nat. Commun. **7**, 11619 (2016).

[52] H. Zhao, X. Qiao, T. Wu, B. Midya, S. Longhi, and L. Feng, Non-Hermitian topological light steering, Science **365**, 1163 (2019).

[53] S. Mittal, V. V. Orre, D. Leykam, Y. D. Chong, and M. Hafezi, Photonic Anomalous Quantum Hall Effect, Phys. Rev. Lett. **123**, 043201 (2019).

[54] S. Afzal, T. J. Zimmerling, Y. Ren, D. Perron, and V. Van, Realization of Anomalous Floquet Insulators in Strongly Coupled Nanophotonic Lattices, Phys. Rev. Lett. **124**, 253601 (2020).

[55] See Supplemental Material at http://link.aps.org/supplemental/10.1103/PhysRevB.106.134112 for scattering matrix model and topological characterization of a spectral winding number.

[56] Z. Zhang, P. Delplace, and R. Fleury, Superior robustness of anomalous non-reciprocal topological edge states, Nature (London) **598**, 293 (2021).

[57] B. Huang and W. V. Liu, Floquet Higher-Order Topological Insulators with Anomalous Dynamical Polarization, Phys. Rev. Lett. **124**, 216601 (2020).

[58] W. Zhu, H. Xue, J. Gong, Y. D. Chong, and B. Zhang, Time-periodic corner states from Floquet higher-order topology, Nat. Commun. **13**, 11 (2022).

[59] D. Smirnova, D. Leykam, Y. D. Chong, and Y. Kivshar, Nonlinear topological photonics, Appl. Phys. Rev. **7**, 021306 (2020).

[60] M. Wimmer, A. Regensburger, M.-A. Miri, C. Bersch, D. N. Christodoulides, and U. Peschel, Observation of optical solitons in PT-symmetric lattices, Nat. Commun. **6**, 7782 (2015).

[61] L.-J. Lang, S.-L. Zhu, and Y. D. Chong, Non-Hermitian topological end breathers, Phys. Rev. B **104**, L020303 (2021).

[62] D. Leykam, M. C. Rechtsman, and Y. D. Chong, Anomalous Topological Phases and Unpaired Dirac Cones in Photonic Floquet Topological Insulators, Phys. Rev. Lett. **117**, 013902 (2016).